Optical Materials 137 (2023) 113547

Contents lists available at ScienceDirect

Optical Materials

journal homepage: www.elsevier.com/locate/optmat

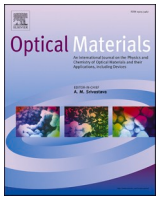

Research Article

Supercontinuum generation in chalcogenide photonic crystal fiber infiltrated with liquid

Lanh Chu Van [a], Khoa Dinh Xuan [a], Trung Le Canh [a], Thanh Thai Doan [b], Thuy Nguyen Thi [c], Hieu Van Le [d], Van Thuy Hoang [a,*]

[a] Department of Physics, Vinh University, 182 Le Duan, Vinh City, Viet Nam
[b] Ho Chi Minh City University of Food Industry, 140 Le Trong Tan, Tan Phu, Ho Chi Minh City, Viet Nam
[c] University of Education, Hue University, 34 Le Loi, Hue City, Viet Nam
[d] Faculty of Natural Sciences, Hong Duc University, 565 Quang Trung Street, Thanh Hoa City, Viet Nam

ARTICLE INFO

Keywords:
Nonlinear fiber
Chalcogenide fiber
Supercontinuum generation
Coherence
Tapered fiber
Liquid infiltration
Group velocity dispersion

ABSTRACT

Chalcogenide fibers have attracted much attention for multi-octave spanning supercontinuum generation in the mid-infrared range. However, readily optimizing the dispersion characteristics as well as other mode properties is still problematic because it is difficult to fabricate chalcogenide fibers with sophisticated structures. In this work, we numerically investigate the liquid infiltration as a post-processing method to optimize the dispersion shapes, so that the nonlinear dynamics and spectro-temporal properties of supercontinuum generation are efficiently controlled. In particular, water, carbon disulfide (CS_2), carbon tetrachloride (CCl_4), and bromoform ($CHBr_3$) are selected to fill into all cladding air holes of $As_{38}Se_{62}$ fibers for dispersion engineering. By pumping a femtosecond laser at 4.5 μm, pulse duration of 250 fs, and pulse energy of 0.1 nJ (peak power of 0.4 kW), the unfilled and CCl_4-filled fibers provide soliton-induced supercontinuum generation with a spectral bandwidth of 2.5–6.5 μm and 2.0–5.5 μm, respectively. Whilst, $CHBr_3$-filled fiber offers all-normal dispersion supercontinuum generation with high coherence and spectral bandwidth of 2.2–5.2 μm. In contrast, unfortunately, CS_2 and water-filled fibers have complex dispersion shapes and provide narrow bandwidth supercontinua. We also thoroughly numerically investigate the tapered fibers, which assure both high coupling efficiency with laser sources and high nonlinearity, for broad mid-infrared supercontinuum generation. The results point out that liquid-filled tapered fibers can provide both anomalous and all-normal dispersion SC generation with an octave-spanning bandwidth via the same value of input peak power (0.4 kW). With a large core diameter (12 μm) at the input and output fiber ends, the tapered fibers have a potential to couple with high-power laser pulses without fiber damage, therefore, they can provide supercontinuum spectra with broad bandwidth and high spectral power density for practical applications in sensing, gas detection, and LIDAR.

1. Introduction

Supercontinuum (SC) generation in an optical fiber is a temporal and spectral broadening of high-power laser pulses via simultaneous dispersion and nonlinearity effects [1]. For a few decades, development of fiber materials and fiber configuration brings about SC generation with broad spectral bandwidth from ultra-violet (UV) up to the mid-infrared (mid-IR) range with high average output power [2]. Nowadays, fiber-based SC sources have been widely applied in inter-disciplinary fields such as optical coherence tomography [3], multi-photon spectroscopy [4,5], and optical frequency metrology [6]. Among the fiber materials, silica has high transparency, high purity, and easy-to-handle for fiber fabrication by using a conventional stack-and-draw method. However, silica fibers only offer SC generation in UV (around 0.37 μm) [7], visible [8], and near-IR ranges (wavelength below 2.4 μm). High attenuation of silica in the mid-IR range limits spectral broadening with longer wavelengths ($\lambda > 2.4$ μm). Because of this, non-silica-based optical fibers have attracted much attention for light guidance and SC generation in the infrared wavelength region. For example, hollow-core fibers infiltrated with gases and liquids (as light guidance media) have been used for broad SC generation from vacuum-UV up to 4 μm [9–12]. The drawbacks of these fibers are

* Corresponding author.
E-mail address: thuyhv@vinhuni.edu.vn (V.T. Hoang).

https://doi.org/10.1016/j.optmat.2023.113547
Received 2 January 2023; Received in revised form 29 January 2023; Accepted 31 January 2023
Available online 6 February 2023

complicated schemes of experimental setups by using gas or liquid reservoirs, and low coupling efficiency with high power delivery fibers (i.e., large mode area solid core fibers [13]) for a compact all-fiber SC system. Gas-filled fibers typically have large effective mode areas, and they require very high input power broadband SC generation [9]. Moreover, the stability of output SC spectra from gas and liquid-core fiber over a long time (a few hours) is still questionable [14].

Solid-core fibers made from soft glasses, such as heavy metal oxide glasses [15,16], tellurite (TeO2-based glass) [17], and chalcogenide [18] have attracted much attention for multi-octave spanning SC generation in visible and IR range. These soft-glass fibers typically have high nonlinearity, and most importantly, high transparency in the mid-IR range [18]. Among the soft glasses, chalcogenide glasses are excellent platforms for SC applications due to their wider transmission window, and hundred times larger nonlinearity compared to that of silica. Recently, a few kinds of chalcogenide glasses (e.g., As_2S_3, As_2Se_3, GeAsSe, and GeAsTeSe) and fiber structures have been developed for mid-IR SC generation with spectral bandwidth up to 18 μm [2,18,19]. The mid-IR SC generation has played an important role in numerous applications, such as gas detection [20], mid-infrared spectroscopy [21], and multispectral photoacoustic microscopy [22].

It is worth noting that nonlinear dynamics for SC generation depend on the mode properties (e.g., group velocity dispersion) [1]. For example, fibers with flat near-zero dispersion can offer broadband SC generation because a phase-matching condition is conserved over the long wavelength range. Fibers with normal dispersion provide SC generation induced by self-phase modulation (SPM) and optical wave breaking (OWB) with a flat-top spectrum, and high shot-to-shot coherence. Fibers with anomalous dispersion provide soliton-induced SC generation with a broad spectral bandwidth, complex spectrogram, and low coherence [1]. In the other words, modification of dispersion characteristics enables to tailoring of spectro-temporal properties of SC generation. For optical fibers, the dispersion depends on the material and fiber structure. In general, the fiber dispersion is significantly controlled by changing fiber parameters, such as core diameter and cladding photonic structure. However, fiber fabrication from the chalcogenide glasses is still a challenge because of crystallization, and high sensitivity of glass viscosity to temperature [18]. This difficulty restricts fabricating a fiber with a sophisticated structure for optimizing dispersion characteristics. Most previous works have considered step-index chalcogenide fibers because of straightforward fiber fabrication, but step-index fibers exhibit limitations of dispersion engineering [18,19,23]. The complex fiber structure may suffer a further fast aging process leading to an increase in fiber attenuation via the absorption of e.g., OH and Se–H group [24,25]. Recently, only a few works have investigated hybrid microstructured chalcogenide fibers for all-normal dispersion (ANDi) SC generation [26], and polarization-maintaining SC generation [27,28].

An interesting method to optimize the dispersion and mode properties of microstructured fibers for SC generation is to fill a selected liquid into air holes in the cladding region. In such a case, the selected liquids typically have lower refractive indices than the host glasses, and thus, the filled-liquid fibers still assure light guidance by total internal reflection (TIR). However, the refractive index profile of the cladding is modified, resulting in the adaptation of dispersion shape and effective mode area for SC generation. Relying upon this concept, Canh et al., have shifted the dispersion shape of a suspended core silica fiber from anomalous to the normal regime by water infiltration for ANDi SC generation with a spectral bandwidth of 0.43–1.33 μm [8]. Le et al., have optimized dispersion characteristics of the lead-bismuth-gallate glass solid-core photonic crystal fiber by filling carbon tetrachloride into the cladding air-holes for ANDi SC generation in the wavelength range of 0.93–2.5 μm [16]. The work reported in Ref. [29] presents dispersion engineering of As_2Se_3 suspended core fiber infiltrated with liquids. However, this work only considers the dispersion in a narrow wavelength range from 2.0 μm to 3.0 μm, while the SC generation in chalcogenide fibers typically broadens to much longer wavelengths (e.g., up to 13 μm [29]). It is also to note that refractive index curves of liquids in the mid-IR range are not smooth, meaning that these curves may suddenly change via stretching and bending modes of liquid molecules, resulting in complex shapes of the fiber dispersion and restriction of spectral broadening. These features should be thoroughly investigated.

In this work, we numerically study microstructured chalcogenide fibers infiltrated with liquids for SC generation. Our results point out that it is possible to optimize the dispersion characteristics of the fibers by filling the selected liquids into cladding air holes. The dispersion can be shifted from anomalous to a normal regime for ANDi SC generation. The linear properties of liquid-filled fibers are meticulously investigated by using the finite-difference method. Next, nonlinear propagation in the selected fibers is numerically simulated by using the split-step method with a femtosecond laser as a pump source. Tapered chalcogenide fibers infiltrated with liquids, which assure high coupling efficiency with laser sources and high nonlinearity for spectral broadening, are also thoroughly investigated for both anomalous and ANDi broad SC generation.

2. Linear properties of liquid-filled chalcogenide fiber

The fiber structure consists of a solid core surrounded by three rings of cladding air holes, as shown in Fig. 1 (a). It is noted that dispersion of photonic crystal fibers significantly depends on the geometrical parameters of inner cladding rings (i.e., the first and second rings from the core). An increase in the number of cladding rings only slightly reduces the confinement loss, and it does not noticeably change the dispersion characteristics.

The fiber is made from $As_{38}Se_{62}$ chalcogenide glass. We consider this glass for the developed fibers because it provides high feasibility to fabricate microstructured fibers with cladding air-holes, and the cross-section of the fiber can be scaled down by using a tapered process [28]. It is worth mentioning that most previous works consider microstructured chalcogenide fibers made from two or three kinds of glasses with their compatible thermo-mechanical properties for fiber drawing. In such fibers, cladding holes are drawn from a glass with lower refractive indices than the host [26,27]; thus, there is no place for liquid infiltration.

We assume that all cladding holes have the same diameter and that the investigated fibers do not exhibit high birefringence. The geometrical parameters of fiber include lattice pitch (Λ), diameter of cladding holes (d), the air hole diameter to the pitch ratio (d/Λ), and core diameter $d_{core} = 2\Lambda\text{-}d$, see Fig. 1 (a).

Refractive index and attenuation of $As_{38}Se_{62}$ glass are extracted in Ref. [28] and shown in Fig. 1 (b). Refractive index is in the range of 2.75–2.8, and higher than refractive indices of the selected liquids, assuring light guidance by TIR in the investigated fibers. $As_{38}Se_{62}$ glass has low attenuation in the wavelength range of 2.0 μm–9.5 μm, and a peak of attenuation at 4.56 μm due to the presence of Se–H chemical bonds.

In this work, we select carbon disulfide (CS_2), carbon tetrachloride (CCl_4), bromoform ($CHBr_3$), and water to fill into all cladding air holes for dispersion engineering. These liquids have clear data of refractive index and attenuation in the mid-IR range (e.g., from 1.0 μm to 9.0 μm) [11,30–33]. CS_2 and CCl_4 have high transparency in the mid-IR range in comparison with other liquids [30–32], this future allows for a significant decrease in fiber loss (leakage light in the cladding region absorbed by the liquids). Water is non-flammable and non-toxic. Its evaporation rate is lower than for popular solvents used in optofluidic. $CHBr_3$ has a flat curve of refractive index in the wavelength range of 1.0–8.0 μm [31], and attenuation in the mid-IR range is also low.

The selected liquids have variations of refractive index curves at some wavelengths related to the stretching and bending mode of the liquid molecules, see Fig. 1 (c). For example, CS_2 has a variation of refractive index curve in the range of 6.4–6.9 μm, water has two

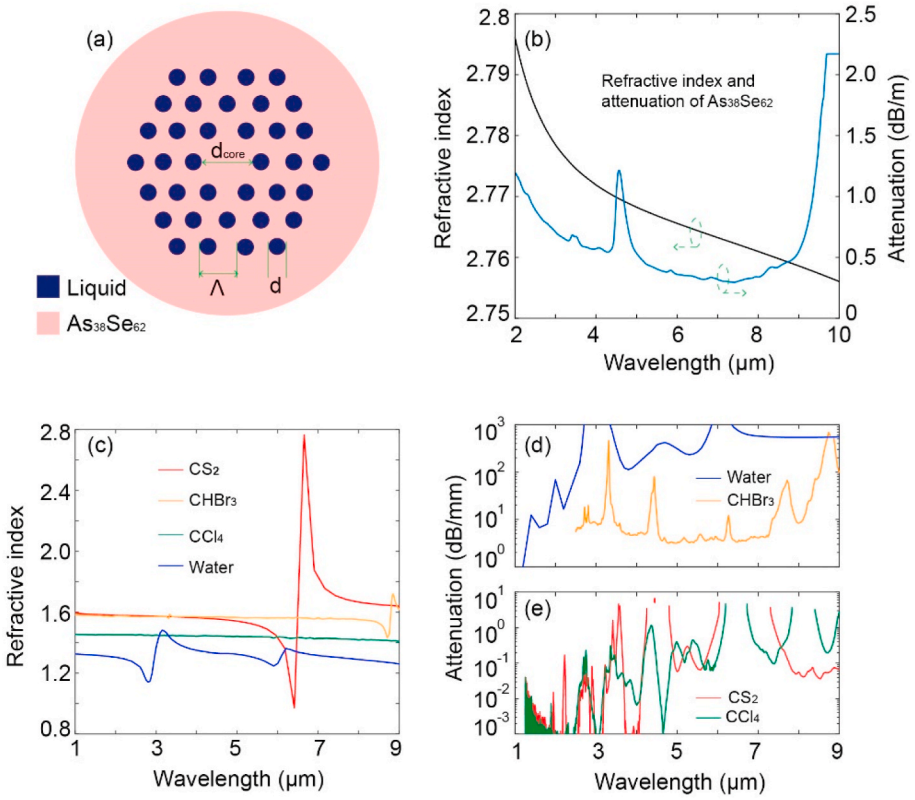

Fig. 1. (a) Schemes of the chalcogenide photonic crystal fiber infiltrated with liquid, (b) refractive index and attenuation of $As_{38}Se_{62}$ glass [28], (c) refractive index of the selected liquids in the mid-IR range [11,30,31], (d) attenuation of water and $CHBr_3$ [30,33], (e) attenuation of CS_2 and CCl_4 [32].

variations around 2.8–3.15 μm and 5.9–6.2 μm, and $CHBr_3$ has two variations around 3.3 μm and 8.8 μm. The refractive index curve of CCl_4 does not show any variation in the investigated wavelength range. The attenuation of the selected liquids is shown in Fig. 1 (d, e). The liquids with high attenuation, such as water, strongly absorb the leakage light in the cladding region, resulting in an increase in fiber loss.

It is possible to fabricate microstructured $As_{38}Se_{62}$ fiber with small values of Λ and d by using a sack-and-draw method in combination with a tapered process. For example, highly birefringent microstructured fibers with $\Lambda = 1.7$ μm and $d/\Lambda \approx 0.5$ are fabricated by the stack-and-draw method for mid-IR SC generation [28]. Therefore, in this work, we numerical analysis of dispersion characteristics of microstructured fibers with $\Lambda = 1.5$–5 μm, and $d/\Lambda = 0.5$. In fact, the values of the ratio d/Λ can be modified by changing gas pressure (e.g., helium) inside the enclosure during the fiber drawing process [28]. Holley core microstructured fibers offer endless single-mode operation with $d/\Lambda < 0.42$ [34]. The single-mode guidance also depends on wavelength, d/Λ, and λ/Λ. In the mid-IR range, a microstructured fiber with factor $d/\Lambda = 0.5$ offers single-mode guidance, meaning that only the fundamental mode can be excited and/or high-order modes quickly disappear from the onset of the nonlinear propagation via their high confinement loss [34]. The small values of the ratio d/Λ lead to an increase in confinement loss and effective mode area, so the nonlinear effects for spectral broadening are strongly decreased. Large values of the ratio d/Λ require high pressure of helium gas inside the enclosure during the fiber fabrication, leading to difficulties in the fiber drawing process and non-uniform cladding air-holes.

The chalcogenide fibers with submicrometer of cladding air holes (e.g., $\Lambda = 1.5$–3 μm) are difficult to fabricate because of the sensitivity of glass viscosity to temperature [18]. However, the proposed fibers can be fabricated by using the tapered process as presented in Ref. [28]. Such a method includes three steps (i) fiber with a large lattice pitch (e.g., $\Lambda \approx 7$ μm): is drawn by fiber tower at 340 °C temperature of the furnace [28]; (ii) the fabricated fiber is subsequently tapered down by using the same fiber tower, allowing scale down a fiber with $\Lambda \approx 7$ μm up to $\Lambda = 1.7$ μm. The ratio d/Λ is not significantly changed during the tapered process [28], but the lattice pitch of the waist part can be adapted by changing the speed and time of the stretching-out process; (iii) the untapered and tapered transition parts are cut off and only the waist part is used for SC generation.

The liquid infiltration into the cladding air holes can be implemented using microfluidic pump systems [16,35–38]. In such a system, the end of the fiber is embedded inside a liquid reservoir, and subsequently, the liquid is filled fully into all cladding air holes by capillary action and/or pressure from the microfluidic pump. The small cladding air holes need a long time for liquid infiltration. However, the use of short fiber samples (e.g., 10 cm) and pressure from the liquid pump system assures that the selected liquid is fully infiltrated into submicrometer cladding air holes as previously presented in Ref. [16].

The microstructured fibers with $\Lambda = 1.5$–5 μm support single-mode operation in the mid-IR range. In fact, a large-core unfilled fiber (e.g., $\Lambda = 5$) can provide two modes at a wavelength of 4.5 μm (a pump wavelength for SC generation as discussed in the below sections). However, fortunately, the fiber losses are 0.9 dB/m and 250 dB/m for the fundamental mode (LP_{01}) and the first high order mode (LP_{11}), respectively. For a given value of ratio d/Λ (e.g., $d/\Lambda = 0.5$), when the value of the lattice pitch is decreased and/or the fiber is filled with liquids, the loss of the high-order mode exponentially increases, leading to the quick disappearance of the high-order mode from the onset of propagation. Therefore, we consider the optical properties of the only fundamental mode in the below section.

Dispersion shapes of the fundamental mode (LP_{01}) in the liquid-filled fibers with various values of lattice pitch are shown in Fig. 2. There are a few noticeable features to point out: (i) all unfilled fibers do not have all-normal dispersion, meaning that unfilled fibers do not offer ANDi SC generation. All normal dispersion is only obtained by liquid infiltration

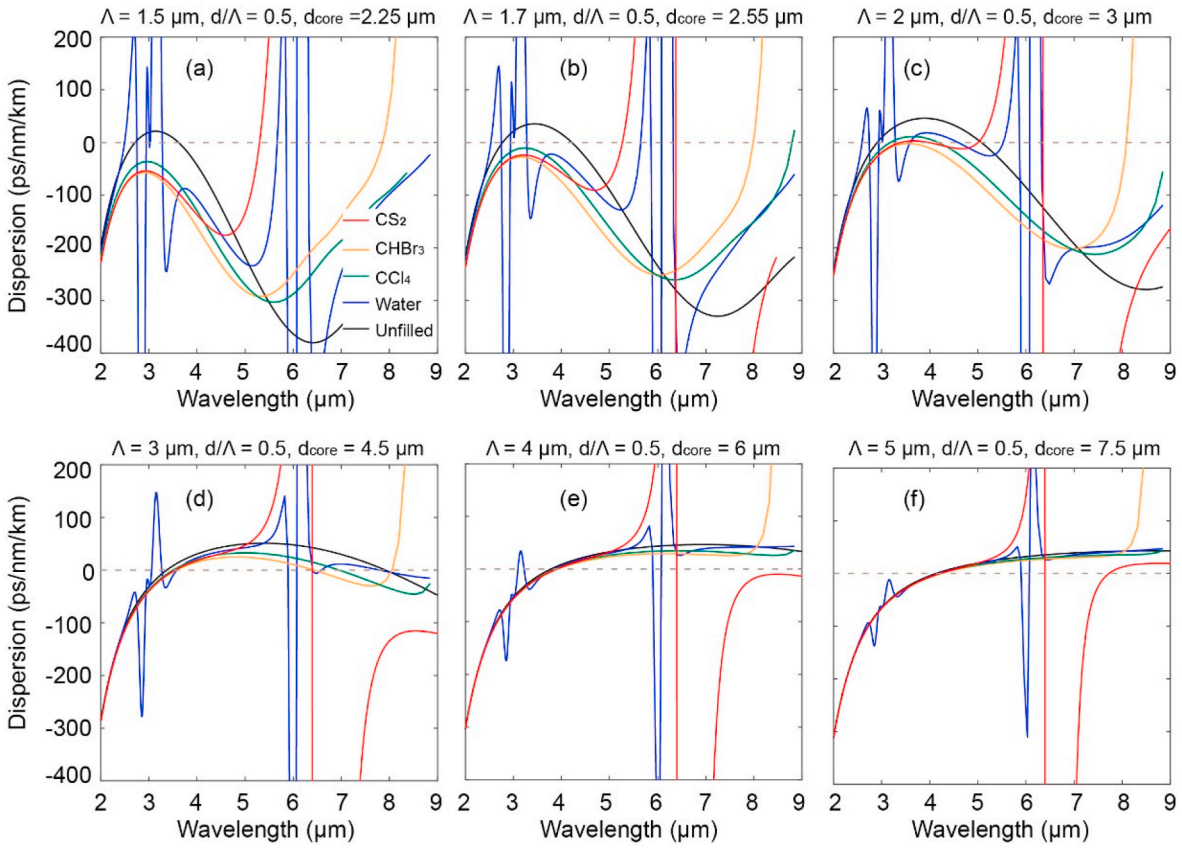

Fig. 2. Dispersion characteristics of $As_{38}Se_{62}$ microstructured fibers infiltrated with the selected liquids. (a) fibers with $\Lambda = 1.5$ μm, (b) $\Lambda = 1.7$ μm, (c) $\Lambda = 2.0$ μm, (d) $\Lambda = 3.0$ μm, (e) $\Lambda = 4.0$ μm, (f) $\Lambda = 5.0$ μm. The ratio $d/\Lambda = 0.5$ for all considered fibers.

into the fibers with small values of lattice pitch (i.e., $\Lambda = 1.5$–2 μm), see Fig. 2(a–c). (ii) dispersion shapes depend on the refractive index profiles of the liquids. For example, dispersion shapes of CS_2 and water-filled fibers have complex variations around 6.5 μm and 3 μm because of the variation of refractive index curves. (iii) dispersion engineering by liquid infiltration is efficient only for small core fibers (i.e., a small value of lattice pitch). For large core fibers, a large part of the input light is guided in the core, and the fiber dispersion follows the material dispersion of $As_{38}Se_{62}$.

Based on the preliminary analysis of dispersion characteristics, the fibers with lattice pitch $\Lambda = 2$ μm ($d_{core} = 3$ μm) are selected for both ANDi and anomalous dispersion SC generation. The proposed fiber infiltrated with $CHBr_3$ has zero-dispersion wavelengths (ZDWs) at 8 μm, and it can offer ANDi SC generation with a pump wavelength of 4.5 μm. Whilst, the unfilled and CCl_4-filled fibers have anomalous dispersion in the wavelength range of 3–5 μm, and they are used for soliton-induced SC generation with a broad spectral bandwidth, see Fig. 2 (c). With the same fiber structure, unfortunately, the fibers with large cores ($\Lambda > 2$ μm) do not have all-normal dispersion in the investigated wavelength, thus they are not an appropriate choice for ANDi SC generation, see Fig. 2(a–f). The fiber with a smaller core (i.e., $\Lambda = 1.5$ and 1.7 μm) also can support both ANDi and anomalous dispersion SC generation, see Fig. 2 (a, b). However, the small core fiber has high confinement loss in the long wavelength range, resulting in a significant reduction of

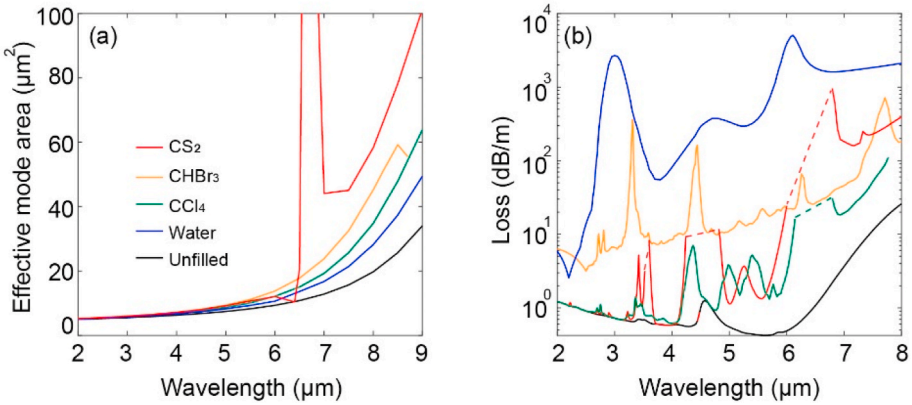

Fig. 3. (a) effective mode areas and (b) loss of the unfilled and liquid-filled fibers. The fiber has $\Lambda = 2$ μm and $d_{core} = 3$ μm. The dashed lines show interpolation values, the fiber loss in accordingly wavelength ranges is not directly calculated because of the lack of data on CS_2 and CCl_4 absorptance in these wavelength ranges in Ref. [32].

intensities at the leading edge of the spectrum. Moreover, if the experimental setup is considered, the small core fiber has a low coupling efficiency with a laser pump.

Effective mode area and loss of the proposed fiber infiltrated with liquids are presented in Fig. 3. Liquid infiltration results in an increase in the average refractive index of the cladding region. Consequently, the effective mode area of liquid-filled fibers is higher than unfilled fiber. CS_2 has a high refractive index at a wavelength of 6.5 μm, leading to a very large effective mode area at this wavelength, see Fig. 3 (a). In addition, liquid infiltration also gives rise the fiber loss because of material absorption. Especially, the water-filled fiber has extremely high loss in the investigated wavelengths (up to 5×10^3 dB/m) via strong absorption of water, and thus, this fiber is not suitable for SC generation. $CHBr_3$-filled fiber has two high peaks of attenuation at 3.3 μm (330 dB/m) and 4.4 μm (140 dB/m), see Fig. 3 (b). However, if short fiber samples (a few centimeters) are used for SC generation, the effect of fiber loss on spectral broadening can be substantially reduced.

3. SC generation in the proposed fibers

SC generation in the proposed fibers is numerically simulated by solving the general nonlinear Schrodinger equation (GNLSE) as given in Eq. (1):

$$\frac{\partial A}{\partial z}+\frac{\alpha}{2}A-\sum_{k\geq 2}\frac{i^{k+1}}{k!}\beta_k\frac{\partial^k A}{\partial T^k}=i\gamma\left(1+i\tau_{shock}\frac{\partial}{\partial T}\right)\times\left\{(1-f_R)|A|^2A+f_RA\times\int h(T-T')|A(T-T')|^2dT'\right\} \quad (1)$$

where $A(z,T)$ is amplitude function of input pulse, α is the loss, β_k is group velocity dispersion and γ is nonlinear coefficient. T is the retarded time frame comoving with A given by $T=t-z\beta_1$. The model includes linear effects (dispersion and loss - shown on the left-hand side of the equation) and nonlinearity (on the right-hand side). In the numerical model, an initial broadband noise (i.e. one photon with random phase per spectral mode) is taken into account [39]. $\tau_{shock}=1/\omega_0$ is the shock time regarding the self-steepening effect. Nonlinear coefficient γ is determined through effective mode area and nonlinear refractive index, $\gamma=2\pi n_2/\lambda A_{eff}$ in which $n_2=8\times10^{-18}$ (m^2/W).

The Raman response function $h(T)$ in Eq. (1) is modeled by a single Lorentzian line and is given by Eq. (2):

$$h(T)=\frac{\tau_1^2+\tau_2^2}{\tau_1\tau_2^2}\exp\left(\frac{-T}{\tau_2}\right)\sin\left(\frac{T}{\tau_1}\right)\Theta(T) \quad (2)$$

where $f_R=0.1$, $\tau_1=23.14$ fs, and $\tau_2=157$ fs have been determined for $As_{38}Se_{62}$ glass [28]. $\Theta(T)$ is the Heaviside step function.

In our modeling, the selected liquids are considered only for dispersion engineering. We preliminary calculate a ratio between evanescent light guided in the cladding liquid (CS_2, for example) and input power. This ratio is 1% around a wavelength of 4.5 μm. Accordingly, the effective nonlinear length of liquid cladding is around 3.2 m (for an input peak power of 0.4 kW). If other liquids, for example, CCl_4 and water with low linear and nonlinear refractive indices are used, the effective nonlinear length of liquid cladding is much longer. This length is very long in comparison with fiber length (4 cm), thus we assume that only the glass as core material contributes significantly to the Kerr and Raman response of the liquid-filled fibers, and nonlinear properties of the liquids are not taken into account. The nonlinear effects of liquid cladding substantially influence on SC generation if very high input peak power is considered, for example, peak power higher than 30 kW for the case of CS_2, or higher than 400 kW for CCl_4.

We numerically investigate the coherence characteristics of SC generation by making use of the usual definitions of first-order coherence $\left|g_{12}^{(1)}(\omega)\right|$ and average coherence $\left|g_{12}^{(1)}\right|$, as described e.g. in Ref. [1]. In our model, we consider the effects of vacuum noise (random phase per input pules) and the amplitude fluctuation of each input pulse compared to the average ones [39–41]. Herein, we assume the root-mean-square of amplitude fluctuation is 1%. We do not consider the effects of polarization noise as this is expected to have only a minor influence by the use of short fiber samples and low input peak power [42–44].

For SC simulation, the input pulses are generated by using single-pass parametric generation in a 10 mm periodically-poled fan-out MgO:$LiNbO_3$ crystal (MgO:PPLN) [28]. The laser pulses have pulse duration of 250 fs, and pulse energy of 0.1 nJ (peak power of 0.4 kW). Indeed, the coupling efficiency in an experimental system with chalcogenide fibers is low (e.g., around 10%). Therefore, the launched peak power of 0.4 kW corresponds to a peak power of 4 kW (i.e., 1 nJ pulse energy) from laser sources. The increase of pulse energy can bring about broad SC bandwidth. However, from an experimental perspective, the proposed fibers have a relatively small core (3 μm), resulting in low coupling efficiency and low input pulse energy launched in the fibers. The high coupling efficiency can be obtained if the large core-tapered fiber is considered as shown in section 4. From the viewpoint of numerical simulation, the SC generation with high input pulse energy (i.e., high peak power) is difficult to numerically simulate with high accuracy because of the limitation of the split-step method. For this method, numerical simulation of SC generation with broad spectral bandwidth requires high resolution in the time domain. In such a case, the simulation is limited by the memory of the computer and computational time.

The pump wavelengths can be tuned in a range of 3–4.5 μm [28]. Although the pump wavelength at 4.5 μm locates at high absorption peak power $As_{38}Se_{62}$ which may result in thermal damage under pump irradiation, this wavelength is near to zero-dispersion wavelengths of the proposed fibers assuring broad spectral broadening. Moreover, the high nonlinearity of the proposed fibers offers board SC generation with low input peak power, and thus, it is possible to significantly mitigate the fiber thermal effects. We also consider SC generation with other pump wavelengths at 3.0, 3.5, and 4.0 μm as shown in Fig. 5.

SC generation in the proposed fibers is presented in Fig. 4. The length of all investigated fibers is 5 cm. The liquid infiltration changes the dispersion characteristics, resulting in tuning the nonlinear propagation and spectro-temporal properties of SC generation. The unfilled fiber has two zero-dispersion wavelengths (ZDWs) at 2.9 μm and 5.07 μm, and the pump wavelength locates at the anomalous dispersion regime. The balance of dispersion and nonlinear effects creates solitons at the onset of the propagation. Soliton number (N) and nonlinear characteristics lengths are calculated as given in Eq. (3):

$$L_D=\frac{t_0^2}{\beta_2},L_{NL}=\frac{1}{\gamma P_0},N=\sqrt{\frac{L_D}{L_{NL}}},L_{fiss}\approx\frac{L_D}{N} \quad (3)$$

where L_D, L_{NL}, and L_{fiss} are dispersion, nonlinear, and soliton-fission lengths, respectively. For an input peak power of 0.4 kW, the soliton number $N=7$, and fission length $L_{fiss}\approx0.9$ cm.

The soliton fission at 0.9 cm of propagation is a result of the effects of high-order dispersion and noise (e.g., vacuum noise). In this context, the onset soliton is ejected into multiple fundamental solitons, and the input pulse is suddenly broadened. At the same time, dispersive waves (i.e., Cherenkov radiation) occur at the trailing and leading edges of the pulses and create the wavelength bands in the normal dispersion regime. Consequently, soliton-induced SC generation in the unfilled fiber has broad spectral bandwidth (from 2.5 to 6.5 μm within 30 dB dynamics). The SC generation has a complex temporal profile and low coherence ($\left|g_{12}^{(1)}\right|=0.7$) via the effects of vacuum noise and amplitude fluctuation of input laser pulses, see Fig. 4(a–c).

The CCl_4-filled fiber has two ZDWs at 3.2 μm and 4.2 μm, and the pump wavelength is in a normal dispersion regime. At beginning of the nonlinear propagation, the input pulse is broadened by SPM. Since the

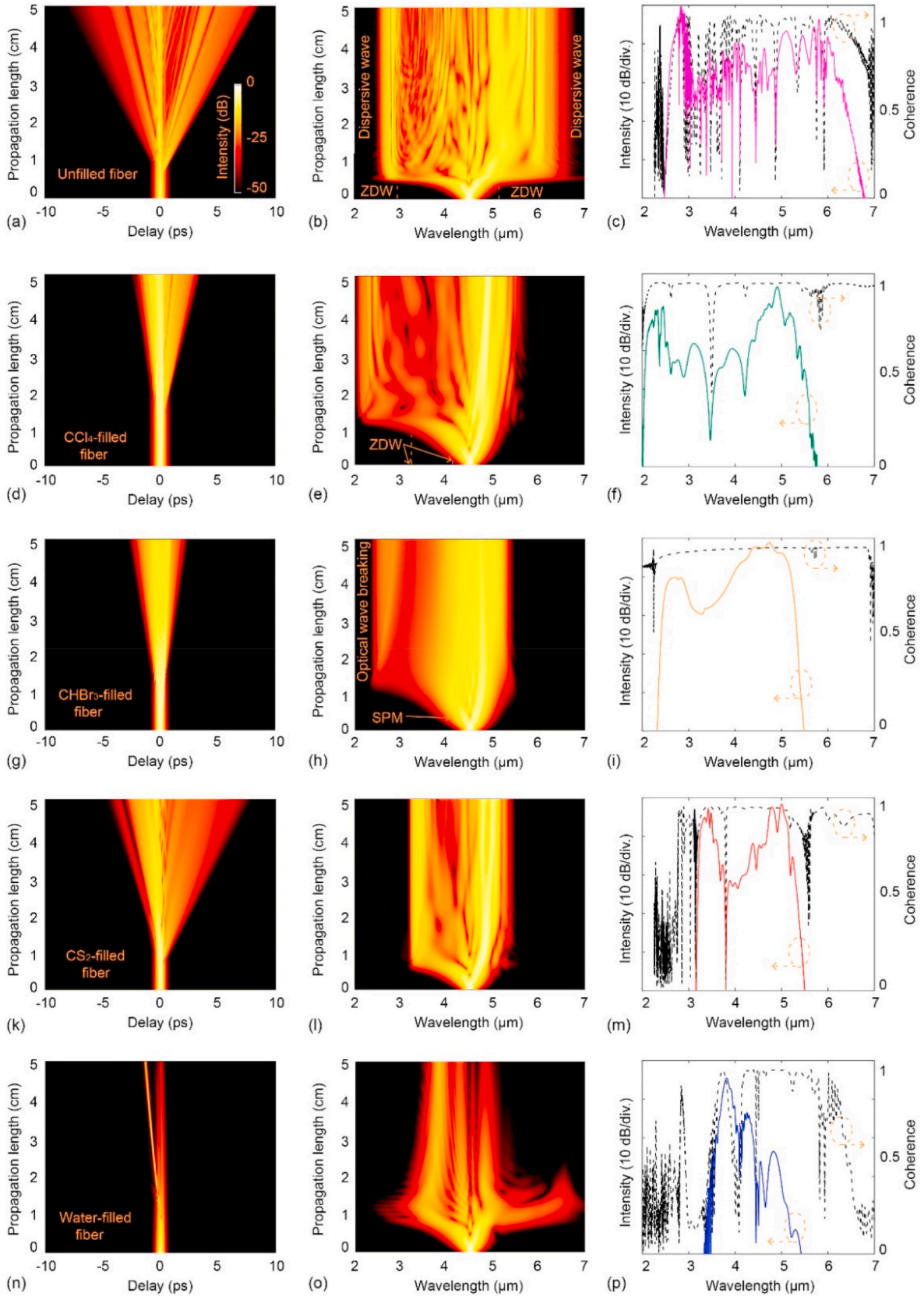

Fig. 4. Pulse evolution, output SC spectrum, and coherence in the investigated fibers. (a, b, c) unfilled fiber, (d, e, f) CCl_4-filled fiber, (g, h, i) $CHBr_3$-filled fiber, (k, l, m) CS_2-filled fiber, and (n, o, p) water-filled fiber. The length of all investigated fibers is 5 cm.

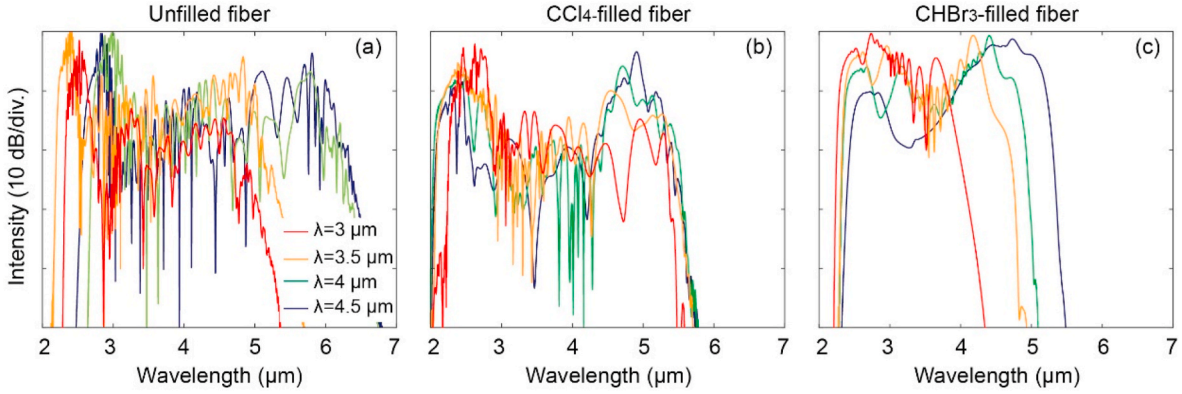

Fig. 5. SC spectra with various pump wavelength is (a) unfilled fiber, (b) CCl_4-filled fiber, and (c) $CHBr_3$-filled fiber. The fiber length is 5 cm and the peak power is 0.4 kW.

pump wavelength is near ZDW (at 4.2 μm), a part of the SPM-induced spectrum is going to access the ZDW and propagates in the anomalous dispersion regime. In such a case, the soliton dynamics contribute to spectral broadening in the anomalous dispersion regime as well as a dispersive wave in the trailing edge of the pulse. Therefore, the SC spectrum has a broad spectral bandwidth of 2.0–5.5 μm within 30 dB. However, the SC spectrum in CCl_4-filled fiber is not flat, and a major part of input light energy locates in the leading edge with negative delays, see Fig. 4(d–f). Although soliton dynamics contribute to the spectral broadening, the SC generation in CCl_4-filled fiber has a high coherence because almost all of the SC spectrum locates in the normal dispersion regime and the vacuum noise is not significantly amplified by modulation instability (MI).

The $CHBr_3$-filled fiber offers all-normal dispersion SC generation induced by SPM and OWB. At the beginning of propagation, SPM is the main contribution to spectral broadening. The SPM-induced spectrum is asymmetry toward the short wavelength because of the effects of the self-steepening effect, thus the OWB occurs clearly in the trailing edge. It is worth mentioning that OWB is a result of four-wave mixing between the SMP-induced components and the pulse tail (wavelength at 4.5 μm), and it only occurs when there is temporal overlap between SMP-induced and pulse tail components. Therefore, during further propagation, no new wavelength is created. The OWB also occurs at the leading edge of the pulse, however, it creates a narrow bandwidth (i.e., 4.9–5.2 μm). The narrow bandwidth of OWB at the leading edge is caused by large effective mode areas at the long wavelengths leading to a decrease in nonlinear effects. Moreover, far-zero and high slopes of the dispersion shape at the long wavelengths result in the limitation of phase-matching conditions. The ANDi SC generation in the $CHBr_3$-filled fiber has a spectral bandwidth of 2.2–5.2 μm within 20 dB and high coherence ($\left|g_{12}^{(1)}\right| = 0.98$), see Fig. 4 (h, i). The temporal profile is smooth and located in the delay from −2.5 ps to 2.0 ps, Fig. 4 (g).

For CS_2 and water-filled fiber, the complex of dispersion shapes restricts the spectral broadening. Especially, a high loss of water-filled fiber critically decreases the output intensities. Therefore, SC generation in these fibers has narrow spectral bandwidth, and complex spectro-temporal profiles, see Fig. 4(k–p)

Supercontinuum generation depends on pump wavelengths that are relevant to the flat of dispersion, soliton number, and nonlinear dynamics of the propagation. For example, Fig. 5 presents output SC generation from the proposed fibers with different values of pump wavelengths. With the same value peak power (0.4 kW) and pulse duration of 250 fs, the laser pumps with central wavelengths at 4.0 and 4.5 μm provide the same spectral bandwidth of SC generation in the unfilled fiber because both wavelengths are near ZDWs and negative slope of dispersion shapes for creating red-shifted DW at the leading edge, see Fig. 5 (a). Whilst, for unfilled and $CHBr_3$-filled fibers, input laser pulses with further short wavelengths ($\lambda < 4.0$ μm) provide narrower spectral bandwidth because the high slope of dispersion shape limits the phase-matching condition, see Fig. 5 (a, c). CCl_4-filled fiber has two ZDWs at 3.2 μm and 4.2 μm, and the dispersion shape is flat with small absolute values in a wavelength range of 3–4.5 μm. Therefore, changing pump wavelength in a range of 3.0–4.5 μm does not significantly reduce the spectral bandwidth, see Fig. 5 (b).

4. SC generation in tapered fiber

Small core fibers typically give rise to high nonlinear coefficients for broad bandwidth SC generation. However, these fibers in turn have low coupling efficiency with laser sources and/or large-mode area fibers for high-power pulse delivery. Consequently, small core fibers are not appropriate to provide SC generation with high spectral power density for practical applications, such as multiphoton imaging techniques and LIDAR. Therefore, in this work, we numerically study SC generation in $As_{38}Se_{62}$ tapered fibers. These fibers have large cores at the untapered parts for high coupling efficiency and a small core at the waist part for a high nonlinear coefficient, see Fig. 6. Lattice pitch for the untapered parts and the waist is 8 μm and 2 μm, respectively. The ratio $d/\Lambda = 0.5$ is assumed as a constant during the tapered process. The core diameter for the untapered parts and the waist are 12 μm and 3 μm, respectively.

The lengths of fiber parts and geometrical parameters of the tapered fibers are shown in Table 1.

Relying on the analysis of nonlinear propagation in the $As_{38}Se_{62}$ fibers as discussed in section 3, the unfilled and $CHBr_3$-filled tapered fibers are used for SC generation. The unfilled tapered fiber is used for anomalous dispersion SC generation, while $CHBr_3$-filled tapered fiber is used for ANDi SC generation.

Linear properties of the tapered fibers are presented in Fig. 7. The unfilled fiber has anomalous dispersion for all of the parameters (Λ = 2–8 μm) and low loss, see Fig. 7 (a, c). The unfilled fibers with Λ = 3–8 μm have similar values of the loss. However, the fiber with Λ = 2 μm (d_{core} = 3 μm) has a much higher loss in the long wavelengths because of the exponential increase in confinement loss, see Fig. 7 (c). The untapered parts have large effective mode areas of 70–80 μm^2 in the investigated wavelengths. The tapered process changes dispersion shapes and decreases the effective mode area. For example, the waist has high slope dispersion shapes and small effective mode areas of 6–20 μm^2, see Fig. 7 (a, b). The $CHBr_3$-infiltration shifts the dispersion toward a normal regime, and especially, the waist part has all-normal dispersion, see Fig. 7 (d). The liquid infiltration increases the refractive index of the cladding region resulting in an increase in effective mode areas and fiber loss, Fig. 7 (e, f). The waist part has a small core, and thus, it offers small effective mode areas in short wavelengths ($\lambda < 6$ μm). However, the small core does not confine the light well in the long wavelength range leading to an exponential increase in effective mode area and

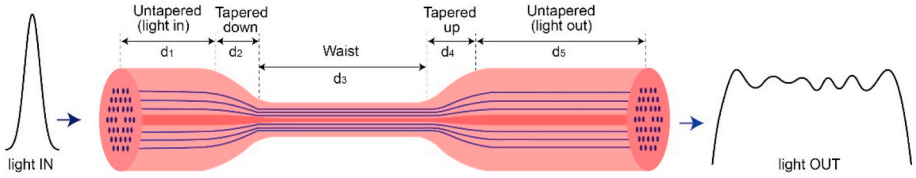

Fig. 6. Schemes of the $As_{38}Se_{62}$ tapered fibers. The fibers include the untapered parts with $\Lambda = 8$ μm and $d_{core} = 14$ μm, the tapered (down and up) transition, and the waist with $\Lambda = 2$ μm and $d_{core} = 3$ μm.

Table 1
Length and parameters of the tapered fibers.

Fiber part	Length (cm)	Lattice pitch (μm)	Core diameter (μm)
Input-light untapered (d_1)	2	8	14
Down-tapered transition (d_2)	2	8 → 2	14 → 3
Waist (d_3)	5	2	3
Up-tapered transition (d_4)	2	2 → 8	3 → 14
Output-light untapered (d_5)	5	8	14

confinement loss.

All linear properties of the tapered fibers are used for SC simulation. We consider the same input laser pulses with a central wavelength of 4.5 μm, pulse duration of 250 fs, and pulse energy of 0.1 nJ for nonlinear propagation in both unfilled and $CHBr_3$-filled fibers.

Nonlinear propagation in unfilled tapered fiber is presented in Fig. 8. The pulse is mainly broadened in the waist part of the fiber by soliton dynamics as discussed in section 3. When the pulses are coupled into the fiber, they locate in the normal dispersion regime of the untapered part. The pulses are very slightly broadened by SPM, and the spectrogram has wings at the trailing edges, see Fig. 8 (a, b, and e). The down-tapered transition has a decrease in the effective mode area and a shift to the anomalous regime of the dispersion. As a result, the pulses are significantly broadened by SPM and soliton fission. Since the pump wavelength is near ZDWs, the spectrum does not experience any substantial delay after propagation in the untapered and down-tapered parts. Thus, the spectrogram at the end of the down-tapered transition has symmetry at 0 (ps), see Fig. 8 (a, c, and g). In the waist part, the pulse is completely broadened via soliton fission, soliton self-frequency shifting, and DW in the normal dispersion regime. The SC generation has broad spectral bandwidth (from 2.5 to 6.5 μm within 30 dB) and a complex structure of the spectrogram, see Fig. 8 (d, h). In the up-tapered transition and output-light untapered parts, the large effective mode area (i.e., low nonlinear coefficient) leads to no noticeable change in spectral broadening. Thus, the spectrum at the end of the fiber and the end of the waist part has a similar spectral structure, see Fig. 8 (h, i). In the time domain, the dispersion effects stretch out the spectrogram, especially the trailing edge of the spectrogram experiences a large delay because of the high value of dispersion at the short wavelength, see Fig. 8 (e). In comparison with non-tapered fiber (i.e., longitudinal uniform fiber with $\Lambda = 8$ μm), the tapered fiber provides SC generation with a much broader spectral bandwidth, see Fig. 8 (i).

For $CHBr_3$-filled tapered fiber, the spectral broadening is induced by SPM at the beginning of the propagation (in the untapered and down-tapered part) with a narrow spectral bandwidth and no substantial delay, see Fig. 9 (c, f). In the waist part, SPM and OWB are the main contributions to spectral broadening, in which OWB creates the new wavelengths at the trailing edge of the pulse (around 2.2 μm). The low nonlinear coefficient in further propagation leads to no further spectral broadening and redistribution of light energy. Thus, spectra at the end of the waist part and the fiber are similar to each other in spectral structure

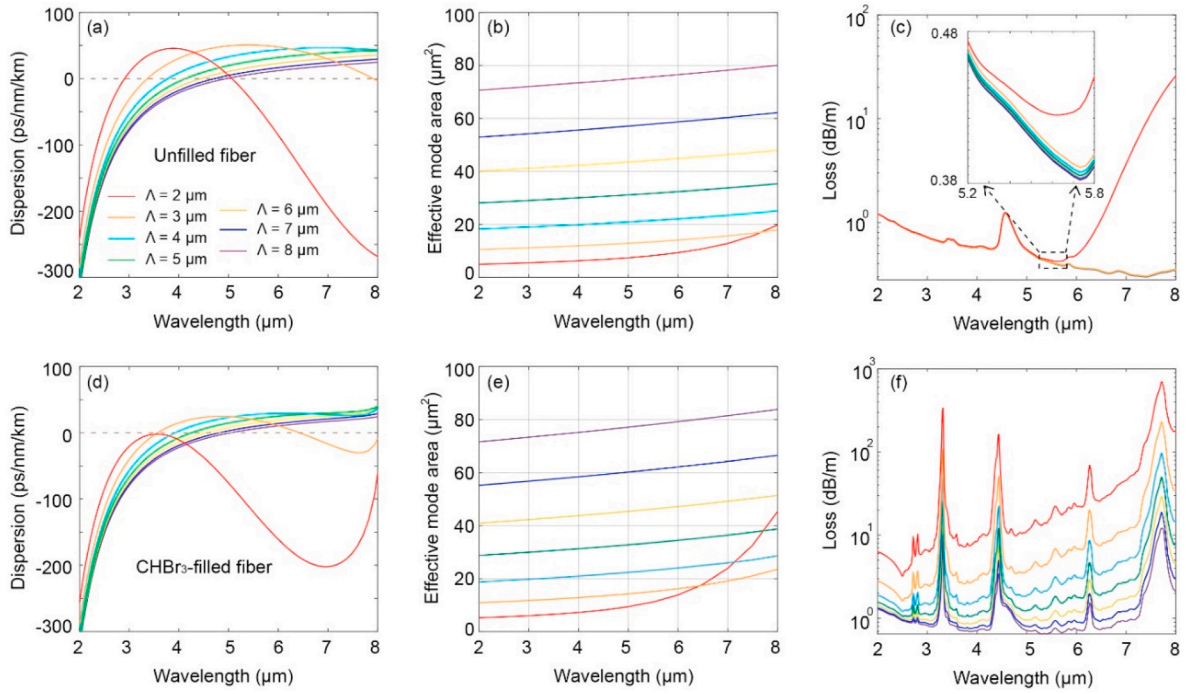

Fig. 7. Linear properties of tapered fiber. For unfilled fiber: (a) dispersion, (b) effective mode areas, and (c) fiber loss. For $CHBr_3$-filled fiber: (d) dispersion, (e) effective mode areas, and (f) fiber loss.

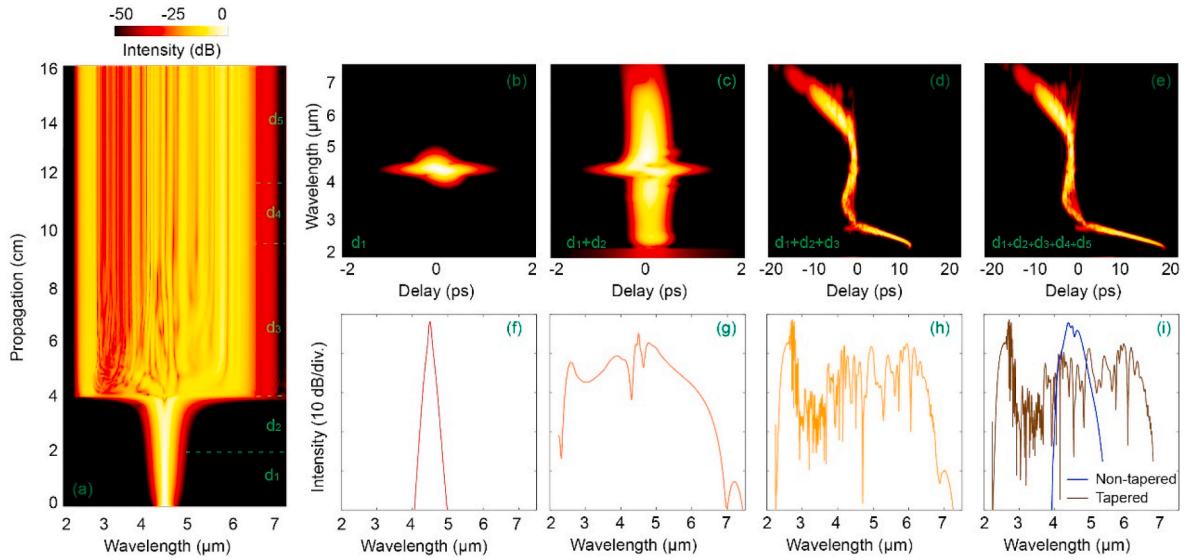

Fig. 8. Supercontinuum generation in unfilled tapered fiber. (a) spectrum evolution. Spectrogram and spectrum at the end of various parts: (b, f) input-light untapered part, (c, g) down-tapered part, (d, h) waist part, and (e, i) output-light untapered part.

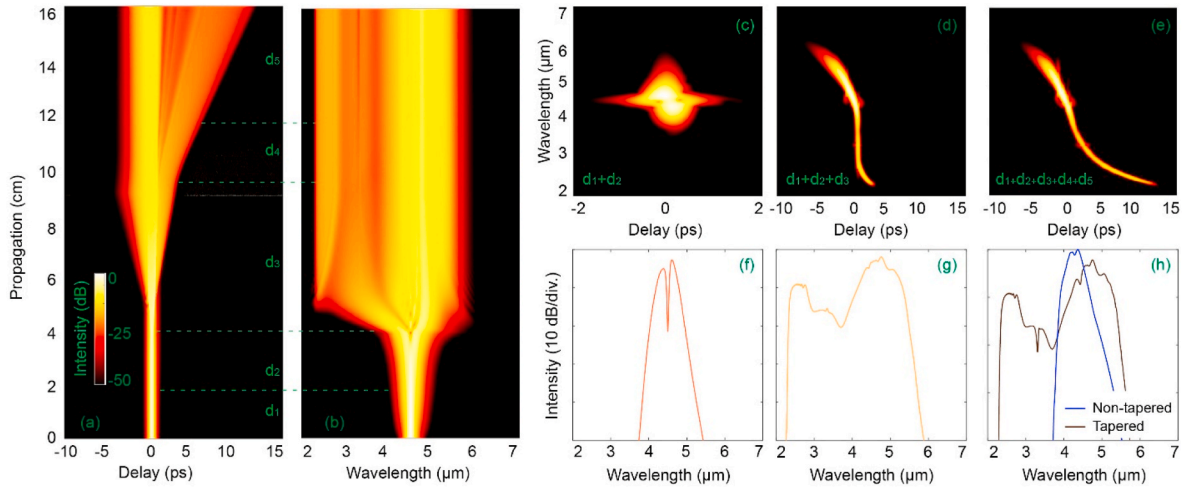

Fig. 9. Supercontinuum generation in $CHBr_3$-filled tapered fiber. (a, b) temporal and spectral evolution. Spectrogram and spectrum at the end of various parts: (c, f) down-tapered part, (d, g) waist part, and (e, h) output-light untapered part.

and bandwidth (from 2.2 to 5.4 μm within 20 dB), see Fig. 9 (b, g, and h). The output spectrum has a decrease in intensity of around 3.2 μm due to the absorption of $CHBr_3$. It is to note that SC generation is induced in the waist part by typical nonlinear dynamics of ANDi SC, however, the leading edge of the spectrum subsequently experiences anomalous dispersion in the up-tapered and output-light untapered parts. Therefore, the temporal profile has a noticeable change at the beginning of the up-tapered part with further delay for the trailing edge, see Fig. 9 (a, d, and e).

Supercontinuum generation in both unfilled and $CHBr_3$-filled tapered fibers is completely spectrally broadened in the waist parts. The tapered-up (d_4) and output-light untapered (d_5) parts do not change the spectral structure of the SC generation. Thus, if only fiber parts from light-input untapered to the end of the waist are used, it is possible to obtain SC generation with high brightness and high spectral power density because no light is absorbed in the tapered-up and output-light untapered parts. A small core of the waist part also assures output SC spectrum with high quality in the spatial distribution, i.e, the bell-shaped distribution in a small area, giving rise to spatial power density for applications in e.g., multiphoton imaging techniques, and liquid/gas detection. However, if an all-fiber system that includes the SC fiber and single-mode fiber to collect and deliver the output SC light is developed, the small core of the waist part provides a low coupling efficiency between the SC fiber with single-mode fiber. In such a case, the tapered-up and the output-light untapered parts should be used for a high coupling efficiency.

In comparison with small core fibers in section 3, the tapered fibers provide the SC generation with the same spectral bandwidth. This feature means that the tapered fibers conserve the nonlinearity as in the small core fibers. At the same time, the tapered fibers assure a high coupling efficiency with laser sources in an experimental setup, enabling the coupling of the laser pulses with much high input power into the fibers without fiber damage and degradation of coupling efficiency over long terms. The tapered fibers provide SC generation with SC bandwidth much broader than non-tapered fiber, Figs. 8 (i) and 9 (h). It is possible to obtain SC with further spectral bandwidth if high pulse energy is launched into the tapered fiber.

An overview of experimental SC generation in chalcogenide fibers is shown in Table 2. The previous works have yielded multi-octave spanning SC generation in anomalous and all-normal dispersion regimes.

However, the broad SC generation requires high peak powers of laser pumps, such as the peak powers in Refs. [23,47,52–54] are at MW level. Ultrashort pulse duration and high pulse peak power are the domain of complex optical parametric chirped-pulse amplification (OPCPA) systems which usually operate with kHz repetition rates. This diminishes the potential of the known coherent supercontinuum pulses in applications involving, e.g., real-time spectroscopy or imaging of dynamic systems. In addition, high peak power may lead to fiber damage via the thermal effects of laser pulses on the input fiber end. In contrast, the proposed fibers can offer SC generation with the same spectral bandwidth in comparison with those in the state-of-the-art with much lower input peak power (0.4 kW). Interestingly, unlike the chalcogenide fibers in the state-of-the-art, the proposed fibers have the flexibility to tailor the dispersion shape by selection and/or replacement of appropriate liquids/mixture toward expected SC generation. Moreover, liquids have noteworthy properties, such as high thermo-optic coefficient, and high birefringence via the effects of external electromagnetic files that can be leveraged to readily control the spectro-temporal properties of SC generation.

The optical properties of the proposed fibers are changed by an aging process that is thoroughly investigated and shown in Refs. [24,25]. The fiber aging is from the diffusion of OH, oxygen, and/or hydrogen inward the chalcogenide glass [25], thus the use of water to fill into the air-holes cladding dramatically changes the optical properties of fibers (i.e., increasing fiber attenuation via absorption of OH and Se–H group), resting in reduction of spectral broadening. The aging evolution of CCl_4, $CHBr_3$, and CS_2-filled fibers may be slower than water-filled fibers because these liquids do not contain the OH group. The aging of the liquid-filled chalcogenide fibers should be thoroughly investigated not only for SC generation but also for application in e.g., sensors and liquid detection. However, we do not implement this research because of a lack of infrastructure in our laboratory.

5. Conclusion

The liquid infiltration to optimize the dispersion characteristics of chalcogenide fibers for SC generation is thoroughly studied. When the cladding air holes are filled with liquids, the refractive index profile of the cladding region is changed, resulting in the shifting of dispersion shape and an increase of effective mode area. Consequently, it is possible to obtain a fiber with further flat, near-near zero dispersion (e.g., CCl_4-filled fiber) and all-normal dispersion (e.g., $CHBr_3$-filled fiber). However, the fibers filled with water and carbon disulfide have a complex shape of dispersion via the variation of the refractive index curve in the mid-IR range. In addition, shifting the dispersion shapes via liquid infiltration is efficient for only small core fibers, such as $d_{core} = 2.25$–3 μm.

Interestingly, relying upon the dispersion modification, it is possible to tailor the nonlinear dynamics for SC generation. For example, we consider the unfilled fiber with $\Lambda = 2$ μm and $d_{core} = 3$ μm for soliton-induced SC generation via input laser pulses with a central wavelength of 4.5 μm, pulse duration of 250 fs, and input peak power of 0.4 kW. This unfilled fiber provides SC generation with broad spectral bandwidth (2.5–6.5 μm). The SC generation is low coherence via the effects of vacuum noise and amplitude fluctuation of input laser pulses. With the same fiber parameters, CCl_4-filled fiber provides the SC generation with a spectral bandwidth of 2.0–5.5 μm and high coherence. The high coherence is understood that a major part of SC generation locates in the normal dispersion regime allowing suppression of the effects of the noises. Especially, ANDi SC generation is obtained in $CHBr_3$-filled fiber with an octave-spanning spectral bandwidth (2.2–5.2 μm). The ANDi SC generation has a high coherence, flat spectrum, and maintained single-pulse in the time domain. In contrast, the CS_2 and water-filled fibers provide the narrow bandwidth SC generation because of their complex dispersion shapes and high attenuation of water in the mid-IR range.

The tapered fibers are also studied in this work for broad SC generation. The untapered and waist parts of these fibers have core diameters of 14 μm and 3 μm, respectively, assuring both high coupling efficiency and high nonlinearity. With an input peak power of 0.4 kW, the unfilled tapered fiber provides the SC generation with a spectral bandwidth of 2.5–6.5 μm, while $CHBr_3$-filled provides ANDi SC generation with a spectral bandwidth of 2.2–5.4 μm.

It is worth noting that it is possible to replace the liquid in the cladding, meaning that liquid infiltration provides a flexible method to optimize dispersion characteristics and mode properties. Therefore, the nonlinear dynamics and spectro-temporal properties of SC generation are readily controlled to meet the requirements of particular applications. For example, broad SC generation in unfilled or CCl_4-filled fibers may be used for mid-IR spectroscopy and detection of gas or gaseous

Table 2
Summary of SC generation in chalcogenide fibers.

#	Glass of core	Pump wavelength (μm)	Peak power (kW)	Spectral bandwidth (μm)	Anomalous /all-normal dispersion	Year of pub.	Ref.
1	As_2S_3	2.6	1.26	1.5–4.4	Anomalous	2013	[45]
2	As_2S_3	2.5	4.86	1.0–4.0	Anomalous	2014	[46]
3	$As_{40}Se_{60}$	6.3	2.29×10^3	1.4–13.3	Anomalous	2014	[23]
4	$Ge_{15}Ga_3Sb_{12}S_{70}$	2.3	40×10^3	0.95–3.35	Anomalous	2015	[47]
5	$Ge_{12}As_{24}Se_{64}$	4	3	1.8–10	Anomalous	2015	[48]
6	As_2S_5	2.7	5.2	2.0–3.3	All-normal	2016	[49]
7	$Ge_{15}Sb_{25}Se_{60}$	6	50	1.8–14	Anomalous	2016	[50]
8	$Ge_{10}As_{22}Se_{68}$	4	16	1–11.5	Anomalous	2017	[51]
9	As_2S_5	10	1.3×10^3	2.0–14	All-normal	2017	[52]
10	As_2Se_3	9.8	2.89×10^3	2–5.1	Anomalous	2017	[53]
11	$Ge_{20}As_{20}Se_{15}Te_{45}$	5.5	126×10^3	1.7–12.7	All-normal	2019	[54]
12	Ge-As-Se-Te	4.65	1.5	2.1–11.5	Anomalous	2019	[55]
13	Ge-As-Se	4	16.5	3.0–6.0	All-normal	2019	[56]
14	$As_{38}Se_{62}$	4.53	2.54	3.1–6.02	Anomalous	2019	[28]
15	$Ge_{20}As_{20}Se_{15}Te_{45}$	5	180	2.0–14	All-normal	2019	[57]
16	$AsSe_2$	2.6	10.12	1.6–3.7	All-normal	2020	[58]
17	As_2S_3	4.2	380	1.7–4.8	Anomalous	2020	[59]
18	As_2Se_3	5	50	2.5–10	All-normal	2020	[26]
19	$As_{39}Se_{61}$	2.45	15	1.4–4.2	Anomalous	2020	[60]
20	$GeSe_4$-$GeTe_4$	8.15	200	1.7–18	Anomalous	2021	[19]
21	As_2S_5	5.3	10	2.0–10	All-normal	2022	[27]
This work ($As_{38}Se_{62}$ fiber infiltrated with liquids)		4.5	0.4	2.5–6.5	Anomalous	Unfilled fiber	
				2.0–5.5	Anomalous	CCl_4-filled	
				2.2–5.2	All-normal	$CHBr_3$-filled	

nerve agent simulants [21,61]. The high coherence ANDi SC generation in $CHBr_3$-filled fiber has the potential to be used for low-noise amplifiers in the mid-IR range, such as Praseodymium-doped and Dysprosium-doped chalcogenide fiber amplifiers [62–64].

CRediT authorship contribution statement

Lanh Chu Van: Methodology, Writing – original draft, Funding acquisition. **Khoa Dinh Xuan:** Validation, Visualization. **Trung Le Canh:** Investigation, Data curation. **Thanh Thai Doan:** Visualization. **Thuy Nguyen Thi:** Investigation. **Hieu Van Le:** Investigation, Data curation. **Van Thuy Hoang:** Conceptualization, Methodology, Writing – original draft, Supervision, Writing – review & editing.

Declaration of competing interest

The authors declare that they have no known competing financial interests or personal relationships that could have appeared to influence the work reported in this paper.

Data availability

No data was used for the research described in the article.

Acknowledgments

This research is funded by Vietnam's Ministry of Education and Training (B2023-TDV-07).

References

[1] J.M. Dudley, G. Genty, S. Coen, Supercontinuum generation in photonic crystal fiber, Rev. Mod. Phys. 78 (4) (2006) 1135–1184, https://doi.org/10.1103/RevModPhys.78.1135.
[2] T. Sylvestre, E. Genier, A.N. Ghosh, P. Bowen, G. Genty, J. Troles, A. Mussot, A. C. Peacock, M. Klimczak, A.M. Heidt, J.C. Travers, O. Bang, J.M. Dudley, Recent advances in supercontinuum generation in specialty optical fibers, J. Opt. Soc. Am. B 38 (12) (2021), https://doi.org/10.1364/JOSAB.439330. F90–F103.
[3] S. Rao D. S, M. Jensen, L. Grüner-Nielsen, J.T. Olsen, P. Heiduschka, B. Kemper, J. Schnekenburger, M. Glud, M. Mogensen, N.M. Israelsen, O. Bang, Shot-noise limited, supercontinuum-based optical coherence tomography, Light Sci. Appl. 10 (2021) 133, https://doi.org/10.1038/s41377-021-00574-x.
[4] C. Poudel, C.F. Kaminski, Supercontinuum radiation in fluorescence microscopy and biomedical imaging applications, J. Opt. Soc. Am. B 36 (2) (2019) A139–A153, https://doi.org/10.1364/JOSAB.36.00A139.
[5] V.T. Hoang, Y. Boussafa, L. Sader, S. Février, V. Couderc, B. Wetzel, Optimizing supercontinuum spectro-temporal properties by leveraging machine learning towards multi-photon microscopy, Front. Photon. 3 (2022), 940902, https://doi.org/10.3389/fphot.2022.940902.
[6] J.T. Woodward, A. W Smith, C.A. Jenkins, C. Lin, S.W. Brown, K.R. Lykke, Supercontinuum sources for metrology, Metrologia 46 (4) (2009) S277, https://doi.org/10.1088/0026-1394/46/4/S27.
[7] A. Hartung, A.M. Heidt, Hartmut Bartelt, Pulse-preserving broadband visible supercontinuum generation in all-normal dispersion tapered suspended-core optical fibers, Opt Express 19 (13) (2021) 12275–12283, https://doi.org/10.1364/OE.19.012275.
[8] T.L. Canh, V.T. Hoang, H.L. Van, D. Pysz, V.C. Long, T.B. Dinh, D.T. Nguyen, Q. H. Dinh, M. Klimczak, R. Kasztelanic, J. Pniewski, R. Buczynski, K.X. Dinh, Supercontinuum generation in all-normal dispersion suspended core fiber infiltrated with water, Opt. Mater. Express 10 (7) (2020) 1733–1748, https://doi.org/10.1364/OME.395936.
[9] A.I. Adamu, Md S. Habib, C.R. Petersen, J.E.A. Lopez, B. Zhou, A. Schülzgen, M. Bache, R. Amezcua-Correa, O. Bang, C. Marko, Deep-UV to mid-IR supercontinuum generation driven by mid-IR ultrashort pulses in a gas-filled hollow-core fiber, Sci. Rep. 9 (2019) 4446, https://doi.org/10.1038/s41598-019-39302-2.
[10] H.L. Van, V.T. Hoang, T.L. Canh, Q.H. Dinh, H.T. Nguyen, N.V.T. Minh, M. Klimczak, R. Buczynski, R. Kasztelanic, Silica-based photonic crystal fiber infiltrated with 1,2-dibromoethane for supercontinuum generation, Appl. Opt. 60 (24) (2021) 7268–7278, https://doi.org/10.1364/AO.430843.
[11] M. Chemnitz, M. Gebhardt, C. Gaida, F. Stutzki, J. Kobelke, J. Limpert, A. Tünnermann, M.A. Schmidt, Hybrid soliton dynamics in liquid-core fibres, Nat. Commun. 8 (2018) 42, https://doi.org/10.1038/s41467-017-00033-5.
[12] V.T. Hoang, R. Kasztelanic, G. Stępniewski, K.D. Xuan, V.C. Long, M. Trippenbach, M. Klimczak, R. Buczyński, J. Pniewski, Appl. Opt. 59 (12) (2020) 3720–3725, https://doi.org/10.1364/AO.385003.
[13] V.T. Hoang, B. Siwicki, M. Franczyk, G. Stępniewski, H.L. Van, V.C. Long, M. Klimczak, R. Buczyński, Broadband low-dispersion low-nonlinearity photonic crystal fiber dedicated to near-infrared high-power femtosecond pulse delivery, Opt. Fiber Technol. 42 (2018) 119–125, https://doi.org/10.1016/j.yofte.2018.03.003.
[14] K. Schaarschmidt, H. Xuan, J. Kobelke, M. Chemnitz, I. Hartl, M.A. Schmidt, Long-term stable supercontinuum generation and watt-level transmission in liquid-core optical fibers, Opt. Lett. 44 (9) (2019) 2236–2239, https://doi.org/10.1364/OL.44.002236.
[15] Z. Eslami, L. Salmela, A. Filipkowski, D. Pysz, M. Klimczak, R. Buczynski, J. M. Dudley, G. Genty, Two octave supercontinuum generation in a non-silica graded-index multimode fiber, Nat. Commun. 13 (2022) 2126, https://doi.org/10.1038/s41467-022-29776-6.
[16] H.V. Le, V.T. Hoang, G. Stępniewski, T.L. Canh, N.V.T. Minh, R. Kasztelanic, M. Klimczak, J. Pniewski, K.X. Dinh, A.M. Heidt, R. Buczyński, Low pump power coherent supercontinuum generation in heavy metal oxide solid-core photonic crystal fibers infiltrated with carbon tetrachloride covering 930–2500 nm, Opt Express 29 (24) (2021) 39586–39600, https://doi.org/10.1364/OE.443666.
[17] M. Klimczak, D. Michalik, G. Stępniewski, T. Karpate, J. Cimek, X. Forestier, R. Kasztelanic, D. Pysz, R. Stępień, R. Buczyński, Coherent supercontinuum generation in tellurite glass regular lattice photonic crystal fibers, J. Opt. Soc. Am. B 36 (2) (2019), https://doi.org/10.1364/JOSAB.36.00A112.
[18] Y. Ohishi, Supercontinuum generation and IR image transportation using soft glass optical fibers: a review, Opt. Mater. Express 12 (10) (2022) 3990–4046, https://doi.org/10.1364/OME.462792.
[19] A. Lemière, R. Bizot, F. Désévédavy, G. Gadret, J.-C. Jules, P. Mathey, C. Aquilina, P. Béjot, F. Billard, O. Faucher, B. Kibler, F. Smektala, 1.7-18 μm mid-infrared supercontinuum generation in a dispersion engineered step-index chalcogenide fiber, Results Phys. 26 (2021), 104397, https://doi.org/10.1016/j.rinp.2021.104397.
[20] M.A. Abbas, K.E. Jahromi, M. Nematollahi, R. Krebbers, N. Liu, G. Woyessa, O. Bang, L. Huot, F.J.M. Harren, A. Khodabakhsh, Fourier transform spectrometer based on high-repetition-rate mid-infrared supercontinuum sources for trace gas detection, Opt Express 29 (14) (2021) 22315–22330, https://doi.org/10.1364/OE.425995.
[21] I. Zorin, P. Gattinger, A. Ebner, M. Brandstetter, Advances in mid-infrared spectroscopy enabled by supercontinuum laser sources, Opt Express 30 (4) (2022) 5222–5254, https://doi.org/10.1364/OE.447269.
[22] M.K. Dasa, G. Nteroli, P. Bowen, G. Messa, Y. Feng, C.R. Petersen, S. Koutsikou, M. Bondu, P.M. Moselund, A. Podoleanu, A. Bradu, C. Markos, O. Bang, All-fibre supercontinuum laser for in vivo multispectral photoacoustic microscopy of lipids in the extended near-infrared region, Photoacoustics 18 (2020), 100163, https://doi.org/10.1016/j.pacs.2020.100163.
[23] C.R. Petersen, U. Møller, I. Kubat, B. Zhou, S. Dupont, J. Ramsay, T. Benson, S. Sujecki, N. Abdel-Moneim, Z. Tang, D. Furniss, A. Seddon, O. Bang, Mid-infrared supercontinuum covering the 1.4–13.3 μm molecular fingerprint region using ultra-high NA chalcogenide step-index fibre, Nat. Photonics 8 (2014) 830–834, https://doi.org/10.1038/nphoton.2014.213.
[24] P. Toupin, L. Brilland, D. Mechin, J. Adam, J. Troles, Optical aging of chalcogenide microstructured optical fibers, J. Lightwave Technol. 32 (13) (2014) 428–2432, https://doi.org/10.1109/JLT.2014.2326461.
[25] M. Jensen, M.M. Smedskjaer, W. Wang, G. Chen, Y. Yue, Aging in chalcohalide glasses: origin and consequences, J. Non-Cryst. Solids 358 (1) (2012) 129–132, https://doi.org/10.1016/j.jnoncrysol.2011.07.041.
[26] H.P.T. Nguyen, T.H. Tuan, L. Xing, M. Matsumoto, G. Sakai, T. Suzuki, Y. Ohishi, Supercontinuum generation in a chalcogenide all-solid hybrid microstructured optical fiber, Opt Express 28 (12) (2020) 17539–17555, https://doi.org/10.1364/OE.394968.
[27] H.T. Tong, A. Koumura, A. Nakatani, H.P.T. Nguyen, M. Matsumoto, G. Sakai, T. Suzuki, Y. Ohishi, Chalcogenide all-solid hybrid microstructured optical fiber with polarization maintaining properties and its mid-infrared supercontinuum generation, Opt Express 30 (14) (2022) 25433–25449, https://doi.org/10.1364/OE.459745.
[28] A.N. Ghosh, M. Meneghetti, C.R. Petersen, O. Bang, L. Brilland, S. Venck, J. Troles, J.M. Dudley, T. Sylvestre, Chalcogenide-glass polarization-maintaining photonic crystal fiber for mid-infrared supercontinuum generation, J. Phys. Photonics 1 (2019), 044003, https://doi.org/10.1088/2515-7647/ab3b1e.
[29] R. Ahmad, Mid-infrared supercontinuum generation in liquid-filled chalcogenide suspended core fiber, Photonics Nanostructures, Fundam. Appl. 52 (2022), 101080, https://doi.org/10.1016/j.photonics.2022.101080.
[30] G.M. Hale, M.R. Querry, Optical constants of water in the 200-nm to 200-μm wavelength region, Appl. Opt. 12 (3) (1973) 555–563, https://doi.org/10.1364/AO.12.000555.
[31] S. Ghosal, J.L. Ebert, S.A. Self, The infrared refractive indices of $CHBr_3$, CCl_4 and CS_2, Infrared Phys. 34 (6) (1993) 621–628, https://doi.org/10.1016/0020-0891(93)90120-V.
[32] S. Junaid, W. Huang, R. Scheibinger, K. Schaarschmidt, H. Schneidewind, P. Paradis, M. Bernier, R. Vallée, S. Stanca, G. Zieger, M.A. Schmidt, Attenuation coefficients of selected organic and inorganic solvents in the mid-infrared spectral domain, Opt. Mater. Express 12 (4) (2022) 1754–1763, https://doi.org/10.1364/OME.455405.
[33] N.I.S.T. WebBook de Chimie. https://webbook.nist.gov/cgi/inchi?ID=C75252&Type=IR-SPEC&Index=1.
[34] M. Koshiba, K. Saitoh, Applicability of classical optical fiber theories to holey fibers, Opt. Lett. 29 (15) (2004) 1739–1741, https://doi.org/10.1364/OL.29.001739.

[35] V.T. Hoang, R. Kasztelanic, A. Anuszkiewicz, G. Stepniewski, A. Filipkowski, S. Ertman, D. Pysz, T. Wolinski, K.D. Xuan, M. Klimczak, R. Buczynski, All-normal dispersion supercontinuum generation in photonic crystal fibers with large hollow cores infiltrated with toluene, Opt. Mater. Express 8 (11) (2018) 3568–3582, https://doi.org/10.1364/OME.8.003568.

[36] V.T. Hoang, R. Kasztelanic, A. Filipkowski, G. Stępniewski, D. Pysz, M. Klimczak, S. Ertman, V.C. Long, T.R. Woliński, M. Trippenbach, K.D. Xuan, M. Śmietana, R. Buczyński, Supercontinuum generation in an all-normal dispersion large core photonic crystal fiber infiltrated with carbon tetrachloride, Opt. Mater. Express 9 (5) (2019) 2264–2278, https://doi.org/10.1364/OME.9.002264.

[37] V.T. Hoang, G. Stępniewski, R. Kasztelanic, D. Pysz, V.C. Long, K.X. Dinh, M. Klimczak, R. Buczyński, Enhancement of UV-visible transmission characteristics in wet-etched hollow core anti-resonant fibers, Opt Express 29 (12) (2021) 18243–18262, https://doi.org/10.1364/OE.426388.

[38] V.T. Hoang, D. Dobrakowski, G. Stępniewski, R. Kasztelanic, D. Pysz, K.X. Dinh, M. Klimczak, M. Śmietana, R. Buczyński, Antiresonant fibers with single- and double-ring capillaries for optofluidic applications, Opt Express 28 (22) (2020) 32483–32498, https://doi.org/10.1364/OE.404701.

[39] P.D. Drummond, J.F. Corney, Quantum noise in optical fibers. I. Stochastic equations, J. Opt. Soc. Am. B18 (2) (2001) 139–152, https://doi.org/10.1364/JOSAB.18.000139.

[40] E. Genier, P. Bowen, T. Sylvestre, J.M. Dudley, P. Moselund, O. Bang, Amplitude noise and coherence degradation of femtosecond supercontinuum generation in all-normal-dispersion fibers, J. Opt. Soc. Am. B 36 (2) (2019) A161–A167, https://doi.org/10.1364/JOSAB.36.00A161.

[41] L.C. Van, T.N. Thi, B.T.L. Tran, D.H. Trong, N.V.T. Minh, H.V. Le, V.T. Hoang, Multi-octave supercontinuum generation in As2Se3 chalcogenide photonic crystal fiber, Phot. Nanostruct. Fundam. Appl. 48 (2022), 100986, https://doi.org/10.1016/j.photonics.2021.100986.

[42] Z. Zhu, T.G. Brown, Polarization properties of supercontinuum spectra generated in birefringent photonic crystal fibers, J. Opt. Soc. Am. B 21 (2) (2004) 249–257, https://doi.org/10.1364/JOSAB.21.000249.

[43] I.B. Gonzalo, R.D. Engelsholm, M.P. Sørensen, O. Bang, Polarization noise places severe constraints on coherence of all-normal dispersion femtosecond supercontinuum generation, Sci. Rep. 8 (1) (2018) 1–13, https://doi.org/10.1038/s41598-018-24691-7.

[44] L.C. Van, B.T.L. Tran, T.D. Van, N.V.T. Minh, T.N. Thi, H.P.N. Thi, M.H.T. Nguyen, V.T. Hoang, Supercontinuum generation in highly birefringent fiber infiltrated with carbon disulfide, Opt. Fiber Technol. 75 (2023), 103151, https://doi.org/10.1016/j.yofte.2022.103151.

[45] W. Gao, M.E. Amraoui, M. Liao, H. Kawashima, Z. Duan, D. Deng, T. Cheng, T. Suzuki, Y. Messaddeq, Y. Ohishi, Mid-infrared supercontinuum generation in a suspended-core As2S3 chalcogenide microstructured optical fiber, Opt Express 21 (8) (2013) 9573–9583, https://doi.org/10.1364/OE.21.009573.

[46] O. Mouawad, J. Picot-Clémente, F. Amrani, C. Strutynski, J. Fatome, B. Kibler, F. Désévédavy, G. Gadret, J.-C. Jules, D. Deng, Y. Ohishi, F. Smektala, Multioctave midinfrared supercontinuum generation in suspended-core chalcogenide fibers, Opt. Lett. 39 (9) (2014) 2684–2687, https://doi.org/10.1364/OL.39.002684.

[47] T. Cheng, H. Kawashima, X. Xue, D. Deng, M. Matsumoto, T. Misumi, T. Suzuki, Y. Ohishi, Fabrication of a chalcogenide-tellurite hybrid microstructured optical fiber for flattened and broadband supercontinuum generation, J. Lightwave Technol. 33 (2) (2015) 333–338, https://doi.org/10.1109/JLT.2014.2379912.

[48] Y. Yu, B. Zhang, X. Gai, C. Zhai, S. Qi, W. Guo, Z. Yang, R. Wang, D. Choi, S. Madden, B. Luther-Davies, 1.8-10 μm mid-infrared supercontinuum generated in a step-index chalcogenide fiber using low peak pump power, Opt. Lett. 40 (6) (2015) 1081–1084, https://doi.org/10.1364/OL.40.001081.

[49] L. Liu, T. Cheng, K. Nagasaka, H. Tong, G. Qin, T. Suzuki, Y. Ohishi, Coherent mid-infrared supercontinuum generation in all-solid chalcogenide microstructured fibers with all-normal dispersion, Opt. Lett. 41 (2) (2016) 392–395, https://doi.org/10.1364/OL.41.000392.

[50] H. Ou, S. Dai, P. Zhang, Z. Liu, X. Wang, F. Chen, H. Xu, B. Luo, Y. Huang, R. Wang, Ultrabroad supercontinuum generated from a highly nonlinear Ge–Sb–Se fiber, Opt. Lett. 41 (14) (2016) 3201–3204, https://doi.org/10.1364/OL.41.003201.

[51] C.R. Petersen, R.D. Engelsholm, C. Markos, L. Brilland, C. Caillaud, J. Trolès, Ole Bang, Increased mid-infrared supercontinuum bandwidth and average power by tapering large-mode-area chalcogenide photonic crystal fibers, Opt Express 25 (13) (2017) 15336–15348, https://doi.org/10.1364/OE.25.015336.

[52] K. Nagasaka, L. Liu, T.H. Tuan, T. Cheng, M. Matsumoto, H. Tezuka, T. Suzuki, Y. Ohishi, Supercontinuum generation in chalcogenide double-clad fiber with near zero-flattened normal dispersion profile, J. Opt. 19 (9) (2017), 095502, https://doi.org/10.1088/2040-8986/aa787b.

[53] T. Cheng, K. Nagasaka, T.H. Tuan, X. Xue, M. Matsumoto, H. Tezuka, T. Suzuki, Y. Ohishi, Mid-infrared supercontinuum generation spanning 2.0 to 15.1 μm in a chalcogenide step-index fiber, Opt. Lett. 41 (9) (2016) 2117–2120, https://doi.org/10.1364/OL.41.002117.

[54] N. Zhang, X. Peng, Y. Wang, S. Dai, Y. Yuan, J. Su, G. Li, P. Zhang, P. Yang, X. Wang, Ultrabroadband and coherent mid-infrared supercontinuum generation in Te-based chalcogenide tapered fiber with all-normal dispersion, Opt Express 27 (7) (2019) 10311–10319, https://doi.org/10.1364/OE.27.010311.

[55] D. Jayasuriya, C.R. Petersen, D. Furniss, C. Markos, Z. Tang, M.D.S. Habib, O. Bang, T. M Benson, A. B Seddon, Mid-IR supercontinuum generation in birefringent, low loss, ultra-high numerical aperture Ge-As-Se-Te chalcogenide step-index fiber, Opt. Mater. Express 9 (6) (2019) 2617–2629, https://doi.org/10.1364/OME.9.002617.

[56] M. Meneghetti, X. Forestier, C.R. Petersen, R. Kasztelanic, M. Klimczak, O. Bang, R. Buczynski, J. Troles, Graded index chalcogenide fibers with nanostructured core, Adv. Photonics Res. 2 (2021), 2000091, https://doi.org/10.1002/adpr.202000091.

[57] K. Jiao, J. Yao, Z. Zhao, X. Wang, N. Si, X. Wang, P. Chen, Z. Xue, Y. Tian, B. Zhang, P. Zhang, S. Dai, Q. Nie, R. Wang, Mid-infrared flattened supercontinuum generation in all-normal dispersion tellurium chalcogenide fiber, Opt Express 27 (3) (2019) 2036–2043, https://doi.org/10.1364/OE.27.002036.

[58] T.S. Saini, T.H. Tuan, T. Suzuki, Y. Ohishi, Coherent mid-IR supercontinuum generation using tapered chalcogenide step-index optical fiber: experiment and modelling, Sci. Rep. 10 (2020) 2236, https://doi.org/10.1038/s41598-020-59288-6.

[59] Z. Eslami, P. Ryczkowski, L. Salmela, G. Genty, Low-noise octave-spanning mid-infrared supercontinuum generation in a multimode chalcogenide fiber, Opt. Lett. 45 (11) (2020) 3103–3106, https://doi.org/10.1364/OL.392282.

[60] S.O. Leonov, Y. Wang, V.S. Shiryaev, G.E. Snopatin, B.S. Stepanov, V. G. Plotnichenko, E. Vicentini, A. Gambetta, N. Coluccelli, C. Svelto, P. Laporta, G. Galzerano, Coherent mid-infrared supercontinuum generation in tapered suspended-core As39Se61 fibers pumped by a few-optical-cycle Cr:ZnSe laser, Opt. Lett. 45 (6) (2020) 1346–1349, https://doi.org/10.1364/OL.386429.

[61] T. Mikkonen, D. Luoma, H. Hakulinen, G. Genty, P. Vanninen, J. Toivonen, Detection of gaseous nerve agent simulants with broadband photoacoustic spectroscopy, J. Hazard Mater. 440 (2022), 129851, https://doi.org/10.1016/j.jhazmat.2022.129851.

[62] L. Sójka, Z. Tang, D. Furniss, H. Sakr, A. Oladeji, E. Bereś-Pawlik, H. Dantanarayana, E. Faber, A.B. Seddon, T.M. Benson, S. Sujecki, Broadband, mid-infrared emission from Pr3+ doped GeAsGaSe chalcogenide fiber, optically clad, Opt. Mater. 36 (6) (2014) 1076–1082, https://doi.org/10.1016/j.optmat.2014.01.038.

[63] M.C. Falconi, G. Palma, F. Starecki, V. Nazabal, J. Troles, J.-L. Adam, S. Taccheo, M. Ferrari, F. Prudenzano, Dysprosium-doped chalcogenide master oscillator power amplifier (MOPA) for mid-IR emission, J. Lightwave Technol. 35 (2) (2017) 265–273, https://doi.org/10.1109/JLT.2016.2632531.

[64] M. Shen, D. Furniss, M. Farries, D. Jayasuriya, Z. Tang, L. Sojka, S. Sujecki, T. M. Benson, A.B. Seddon, Experimental observation of gain in a resonantly pumped Pr3+-doped chalcogenide glass mid-infrared fibre amplifier notwithstanding the signal excited-state absorption, Sci. Rep. 9 (1) (2019), 11426, https://doi.org/10.1038/s41598-019-47432-w.